中國機械工程學刊第四十五卷第一期第 1~10 頁(民國一百一十三年)
Journal of the Chinese Society of Mechanical Engineers, Vol.45, No.1, pp 1~10 (2024)

Effects of Strain Rate and Temperature on Deformation Behaviour and Microstructural Evolution of Powder Metallurgical High-speed Steel (ASP 60) Part 2 – Microstructural Study

Woei-Shyan Lee* and Ting-Ju Chen **

Keywords: high strain rate deformation, negative strain rate sensitivity, dislocation multiplication, lath martensite, secondary precipitation

ABSTRACT

The impact behaviour and quasi-static state deformation of powder metallurgical high-speed steel ASP 60 are investigated at strain rates of 10^{-3} ~ 10^{0} s^{-1} using a material testing system and 2.5×10^{3} ~ 6.0×10^{3} s^{-1} using a split-Hopkinson pressure bar under temperatures ranging from -195°C ~ 1000°C. The results show that the flow stress under dynamic impacts generally increases with decreasing temperature and increasing strain rate. However, a negative strain rate sensitivity occurs at certain strain rates and temperatures due to the high interfacial area of the powder metallurgic structure of ASP 60. The microstructural observations reveal the presence of fine precipitates and dislocation multiplications at -195 ~ 25°C and 2.5×10^{3} ~ 6.0×10^{3} s^{-1}, which result in a high flow resistance of the deformed material. Under both dynamic impacts and quasi-static deformation, the dislocation density is sensitive to the deformation temperature and strain rate. However, the precipitations in the dynamic impact specimens are finer than those in the quasi-static state specimens. Finally, the relationship between the microstructure and mechanical behaviour of the ASP 60 specimens is well described by the work hardening stress, which increases linearly with the square root of the dislocation density..

INTRODUCTION

ASP 60 is a high alloyed high-speed steel (HSS) of the powder metallurgy ASP series. It has good wear resistance and high compressive strength and is regarded as a promising material for cold work tooling due to its lower propensity toward chipping and cracking than conventional carbide-based materials (ASSAB Group, 2020).

The microstructure of ASP 60 was first investigated by Andrén (1981). Thereafter, various critical studies of the precipitation behaviour of ASP 60 were conducted, including those of Stiller et al. in (1984) and Wang et al. (1991). The results indicated that the mechanical properties of ASP 60 are highly sensitive to the microstructure. The high alloying contents of Cr, Mo, W and V in ASP 60 result in a high volume fraction of fine and dense secondary carbide precipitates, which contribute significantly toward its high hot hardness and good wear resistance. Moreover, the primary carbides in ASP 60 are around 10 times larger than those in M2 steel by volume fraction, which results in a greater number of resistance structures in ASP 60 than in general HSS materials.

The mechanical characteristics of ASP 60 have been widely investigated in recent decades. Gomes et al. (1995) examined the fracture behaviour of ASP 60 under 4-point bending at room temperature. Tso et al. (1999) investigated the grinding modes and properties of ASP 60. In a more recent study, Chang et al. (2016) investigated the wear and corrosion properties of oxynitriding-treated ASP 60.

These studies have shown that ASP 60 has many favourable mechanical properties, including high hardness, high strength, and good wear resistance. However, the effects of the strain rate and temperature on the deformation behaviour of ASP 60 are still not yet fully clear. High strain rate deformation occurs in multiple manufacturing processes, including cutting (104 s-1), drawing, stamping, and forging (103 s-1). Creep under quasi-static deformation also commonly occurs during component formation. Moreover, variations of the strain rate and temperature have significant effects on the behaviours of many materials (Hull, 2011). ASP 60 components are often

Paper Received October 2023. Revised November, 2023. Accepted December, 2023. Author for Correspondence:Woei-Shyan Lee.

** Distinguished Professor, Department of Mechanical Engineering, National United University, Miaoli, Taiwan 360302, ROC.*

***Graduate Student, Department of Mechanical Engineering, National Cheng Kung University, Tainan, Taiwan 70101, ROC.*

manufactured by machine cutting and forming processes with high strain rates and a wide range of temperatures. Therefore, it is necessary to understand the deformation behaviour and microstructural evolution of ASP 60 under different strain rates and temperatures in order to optimize the manufacturing conditions.

According to previous studies (Follansbee, 1988), the deformation of metals and alloys may be dominated by several different mechanisms, depending on the particular strain rate and temperature under which the material is processed. For example, for applied strain rates lower than 5×10^3 s^{-1}, the deformation process is dominated by a thermal activation mechanism, in which the flow stress increases with increasing strain rate and decreases with increasing temperature. By contrast, for applied strain rates greater than 5×10^3 s^{-1}, the deformation process is governed by a dislocation drag mechanism, in which the dislocations in the microstructure are provided with sufficient energy to overcome short-range barriers to motion without the need for thermal activation (Lee, 2006). At elevated temperatures, the dislocations in the microstructure experience a high thermal activation energy, which results in their decay or annihilation and a subsequent softening of the material (Lee, 2008). However, at the same time, thermally-induced precipitations increase the resistance to dislocation movement, and hence strengthen the material.

Besides the effects of the strain rate, temperature and precipitates, the deformation behaviour of ASP 60 is also heavily influenced by its powder metallurgic structure. In general, nanoscale particles nucleated from vapor phase contain a higher level of interfacial energy than bulk crystals, and lead to distinctive mechanical properties as a result (German, 1994). The deformation behaviour of ASP 60 thus reflects the outcome of a complex interaction between the effects of the applied strain rate, temperature, and material porosity, respectively.

Accordingly, the present study investigates the effects of the strain rate and temperature on the flow stress and microstructure evolution of ASP 60 at strain rates ranging from 1.0×10^{-3} to 6.0×10^3 s^{-1} and temperatures ranging from -195°C to 1000°C using an MTS 810 universal testing machine and compressive split-Hopkinson bar (SHPB). The residual microstructures of the deformed specimens are observed via transmission electron microscopy (TEM) and energy-dispersive X-ray spectroscopy (EDX). The observation results are then used to interpret the measured mechanical responses of the specimens under the different deformation conditions.

EXPERIMENTAL PROCEDURE

Powder metallurgy grade high-speed steel ASP 60 was purchased from ASSAB Co., Ltd, Taiwan. The material was produced via the hot isostatic pressing (HIP) of gas atomized powders and had a chemical composition (wt.%) of 2.3 C, 4.2 Cr, 7.0 Mo, 6.5 W, 6.5 V, and 10.5 Co. The HIP material was annealed at a temperature of 850-900°C, cooled in the furnace at a rate of 10°C / h to 700°C, allowed to cool naturally to room temperature, and then tempered three times for 1 h at 560°C. The hardness of the final material was HRC 63.10, while the porosity (as measured by the Archimedes water immersion technique) was 7.8 %. The ASP 60 material was received in the form of plates and was roughly machined into cylindrical specimens with dimensions of 7.1 mm × 7.1 mm (diameter x length) using a wire electrical discharge machine (WEDM). The specimens were finished to a final size of 7±0.01 mm × 7±0.01 mm via a centreless grinding operation to remove any surface defects.

The dynamic impact tests were performed using a compressive SHPB (Lee, 2006) at strain rates of 2.5×10^3, 4.0×10^3 and 6.0×10^3 s^{-1}, respectively, and temperatures of -195°C, 25°C, 400°C, and 800°C. The propagation of the incident (ε_i), transmitted (ε_t) and reflected (ε_r) stress waves was measured using two surface-mounted strain gauges mounted at the midpoints of the incident and transmitted bars, respectively, and was displayed in real time on an oscilloscope. The true strain (ε_s), strain rate ($\dot{\varepsilon}_s$) and true stress (σ_s) were derived from one-dimensional wave propagation theory as follows (Lee, 2014):

$$\varepsilon_s=\frac{-2C_0}{L}\int_0^t \varepsilon_r dt \tag{1}$$

$$\dot{\varepsilon}_s=\frac{-2C_0}{L}\varepsilon_r \tag{2}$$

$$\sigma_s=\frac{EA}{A_s}\varepsilon_t \tag{3}$$

, where C_0 is the wave propagation velocity, L is the specimen length, E is the Young's modulus of the bar material, A is the cross-sectional area of the bars, and A_s is the cross-sectional area of the specimen.

The quasi-static deformation tests were conducted using an MTS 810 universal testing machine (MTS Corp., USA) at strain rates of 1.0×10^{-3}, 1.0×10^{-1} and 1.0×10^0 s^{-1}, respectively, and temperatures of 25ºC, 700ºC, 800ºC and 1000ºC. The deformation of the specimens during the compression tests was measured using an optical scale mounted on the hydraulic cylinder of the test system. The resistance force (F) of the specimens was measured using a load cell. The specimen deformation was assumed to be isotropic, i.e., the flow stresses vertical to the compression direction were unrestricted by surface friction, and the strain in any section was constant. The true strain (ε_t), strain rate ($\dot{\varepsilon}_t$), and true stress (σ_t) were therefore evaluated as follows:

$$\varepsilon_t = \int_{L_0}^{L} \frac{dL}{L} = \ln\left(\frac{L}{L_0}\right) \quad (4)$$

$$\dot{\varepsilon}_t = \frac{d\varepsilon}{dt} = \frac{dL/dt}{L} = \frac{V}{L} \quad (5)$$

$$\sigma_t = \frac{F}{A_t} = \frac{4F}{\pi D^2} = \frac{4FL}{\pi D_0^{\,2} L_0} \quad (6)$$

, where F is the applied compressive force, A_t is the instantaneous cross-sectional area of the specimen, D is the instantaneous diameter, D_0 is the original diameter of the specimen, L_0 is the initial height of the specimen, and L is the final height of the specimen.

The microstructure features of the specimens were examined using a JEOL TEM-3010 Analytical Scanning Transmission Electron Microscope (TEM) equipped with a Link eXL-II Energy Dispersive X-ray Analysis System and an image-intensified CCD camera. To obtain TEM foil samples, the deformed specimens were sliced into thin layers with a thickness of 0.3 mm using an automatic metallographic cutting machine. The slices were finished manually and were then polished with a twin jet electropolisher (Struers TenuPol-3) in a solution of 10% perchloric acid, 15% glycerol and 75% ethanol with a voltage of 15 V DC and a sub-zero temperature of -25°C. Figure 1 presents TEM images of the undeformed ASP 60 material, in which the fine secondary carbides and large primary carbides characteristic of ASP 60 (Rong, 1992) are clearly seen. Figures 2(a) and 2(b) present the chemical compositions of the precipitates in Figs.1(b) and 1(c), respectively.

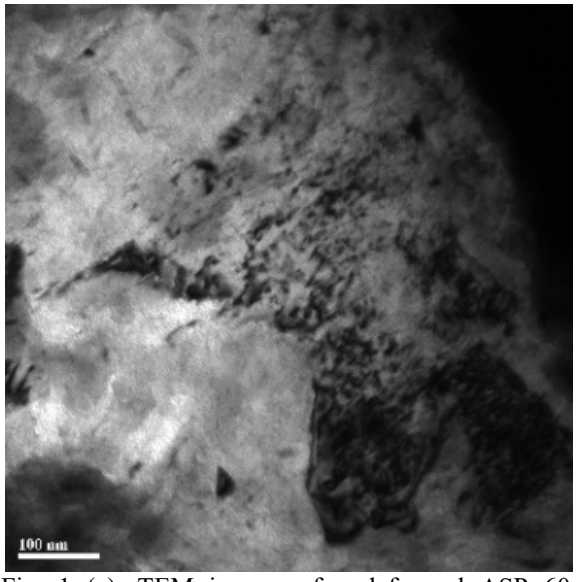

Fig. 1 (a). TEM images of undeformed ASP 60: dense dispersion of fine sphere secondary carbides

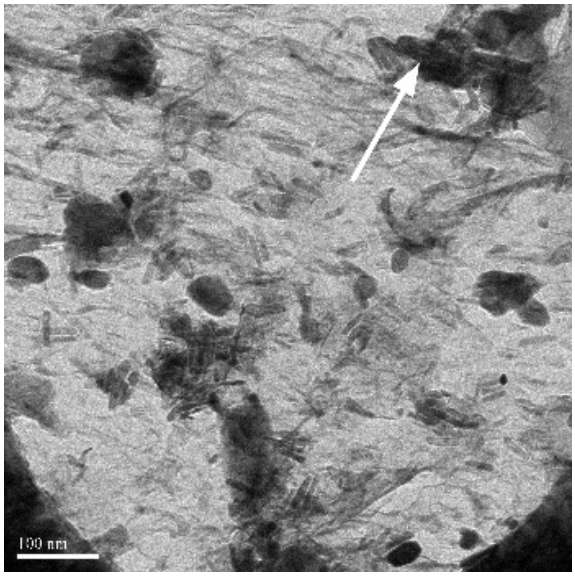

Fig. 1 (b). TEM images of undeformed ASP 60: plate-like and rod-like secondary carbide precipitates formed during tempering.

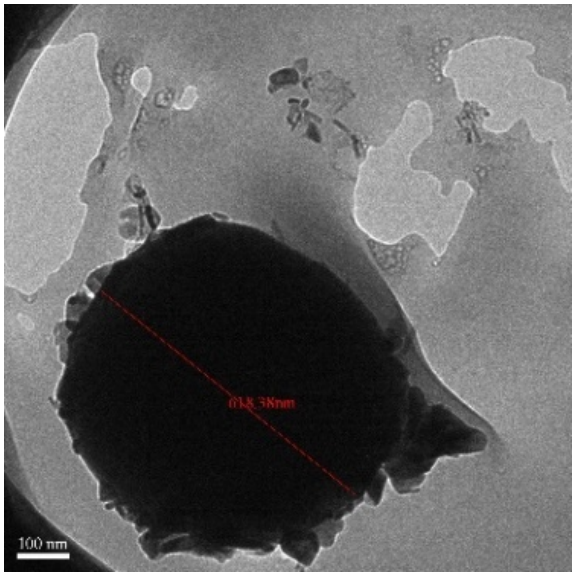

Fig. 1 (c). TEM images of undeformed ASP 60: large primary carbides rich in V and Mo.

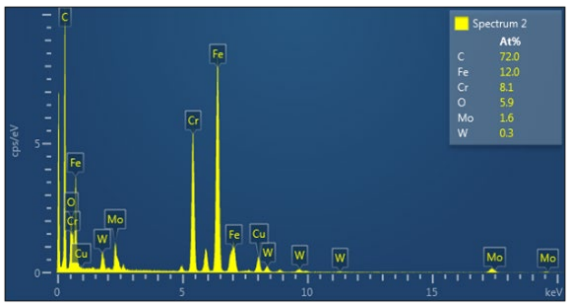

Fig. 2 (a). Chemical compositions of precipitates in Fig.1(b).

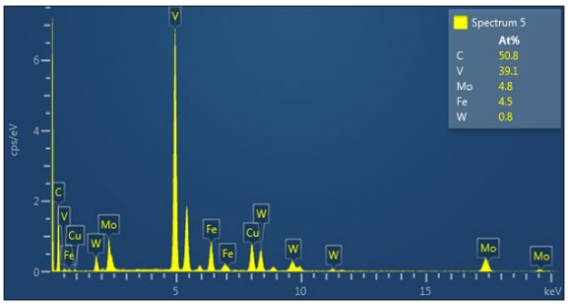

Fig. 2 (b). Chemical compositions of precipitates in Fig.1(c).

RESULTS and DISCUSSION

True stress-strain curves

Figures 3(a) and 3(b) show the true stress-strain curves of the ASP 60 specimens deformed at strain rates of 2500 and 4000 s^{-1}, respectively, and temperatures of -195°C, 25°C, 400°C and 800°C. The results indicate that the ASP 60 specimens possess a high flow stress. For a strain rate of 2500 s^{-1} (Fig. 3(a)), the flow stress reaches the maximum value (2743 MPa) in the specimen impacted at a temperature of -195°C. However, the sample fractures at a low strain of 0.042 due to low-temperature brittleness. By contrast, the specimen tested at 25°C demonstrates a higher flow stress and reaches a final value of 2604 MPa without fracturing or cracking. For a strain rate of 4000 s^{-1} (Fig. 3(b)), the flow stress reaches 2959 MPa at a temperature of 25°C and remains above 1825 MPa for both elevated temperatures. Overall, the flow stresses of ASP 60 are high but depend strongly on both the temperature and the strain rate.

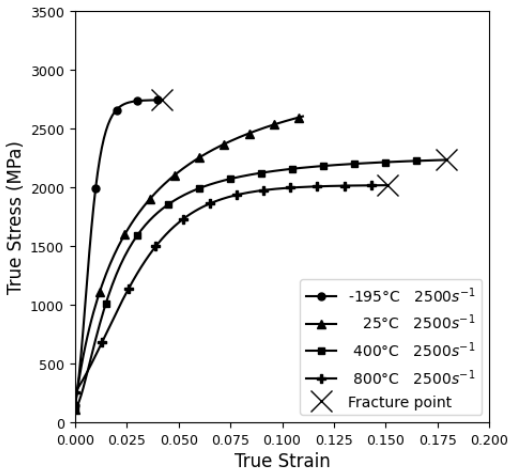

Fig. 3 (a). True stress-strain curves of ASP 60 deformed at various temperatures and strain rates of 2500 s^{-1}.

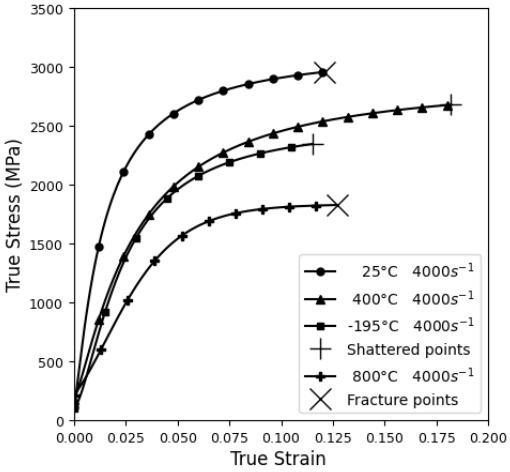

Fig. 3 (b). True stress-strain curves of ASP 60 deformed at various temperatures and strain rates of 4000 s^{-1}.

In addition to the temperature and strain rate, the flow stresses of ASP 60 are strongly affected by its high interfacial area arising from the powder metallurgy process used in its production. As shown in Fig. 3(b) for a strain rate of 4000 s^{-1}, the strength of the ASP 60 specimen reduces significantly at a temperature of -195°C, and is lower than that of the specimens deformed at 25°C and 400°C, respectively, indicating a negative strain rate sensitivity. However, at a lower strain rate of 2500 s^{-1} (Fig. 3(a)), the strength increases consistently with decreasing temperature as a result of thermal activation. Comparing Figs. 3(a) and 3(b), it is seen that when the applied strain rate is increased from 2500 s^{-1} to 4000 s^{-1}, the flow stress increases at temperatures of 25°C and 400°C but decreases at temperatures of -195°C and 800°C. The negative strain rate sensitivity at extremely high and low temperatures can be attributed to the high interfacial brittle characteristic of ASP 60, which results in interfacial instability.

The microstructure of materials depends strongly on the strain, strain rate and temperature. However, a higher deformation degree may lead to thermal softening since the heat produced by the plastic work enhances the possibility of thermal activation, which then provides the dislocations with sufficient energy to overcome short-range barriers to motion. Dislocation multiplication is consequently suppressed. As a result, the effect of work hardening on the plastic deformation mechanism is reduced, and the flow stress increases at a more moderate rate as the strain increases.

The final deformation behaviour of ASP 60 reflects a complex competition effect between the strain, strain rate, temperature, and powder metallurgic nature of the material. In general, however, an increasing strain and strain rate contribute to an improved material strength, while an elevated temperature leads to a lower strength.

Microstructures of ASP 60 Samples Subject to Dynamic Impact

The TEM image in Figure 4(a) shows that the microstructure of the ASP 60 specimen tested at a temperature of -195°C and strain rate of 2500 s^{-1} contains a high density of dislocation structures. The dislocations tangle with the precipitates at the boundaries of the martensite laths (Stiller, 1984). As the strain rate increases, the dislocation density reduces, as shown in the specimen tested under a strain rate of 6000 s^{-1} (Fig. 4(c)). However, at a higher temperature of 25°C, the dislocations increase with increasing strain rate, as evidenced by comparing Figure 5(b) for a strain rate of 4000 s^{-1} and Figure 5(a) for a strain rate of 2500 s^{-1}. Similarly, for a temperature of 400°C, Figure 6(b) shows more severe clusters of tangling dislocations at a strain rate of 4000 s^{-1} than at a strain rate of 2500 s^{-1} (Figure 6(a)). However, for the highest test temperature of 800°C, the number of dislocations decreases as the strain rate increases, as shown in Figure 7(a) for a strain rate of 2500 s^{-1} and Figure 7(b) for a strain rate of 4000 s^{-1}. In other words, the strain rate dependence of the dislocation microstructure at a temperature of 800°C is consistent with that of the samples tested at -195°C (Fig. 4). Overall, the TEM observations in Figs. 4~7 reveal that the number of dislocations in the ASP 60 microstructure reduces with an increasing temperature during dynamic impacts.

The laths of martensite in the ASP 60 microstructure (Stiller, 1984) also reduce as the temperature increases. At a temperature of -195°C (Fig. 4), the dislocations show heavy multiplication within the lathes, and dislocation tangling occurs at the boundaries of the martensite in random directions. At a temperature of 25°C (Fig. 5), laths of martensite can still be seen at both strain rates (2500 and 4000 s^{-1}). However, as the temperature increases to 400°C (Fig. 6), these laths disappear. Meanwhile, rod-like precipitates are seen, which form in particular orientation directions. A similar tendency is observed under the maximum deformation temperature of 800°C at strain rates of 2500 s^{-1} and 4000 s^{-1} (Figs. 7(a) and 7(b), respectively).

The TEM observations indicate that the high hardness and toughness of ASP 60 under dynamic impacts are primarily due to clusters of dislocations and a dense dispersion of fine secondary precipitates. In particular, the extremely fine secondary dispersion of MC and M_2C carbides (Stiller, 1984) poses additional barriers to dislocation motion, which increase the strength and result in a high flow stress of more than 1825 MPa at elevated temperatures. Note that while no typical shock-induced cellular dislocations are found in the TEM images, numerous pores can be seen in the microstructures. Pores are weak points and give rise to localized stress concentrations (German, 1994). As a result, fracture occurs before the onset of mechanical twinning or the formation of dislocation cells in the bcc α-ferrite matrix (Härle, 1993).

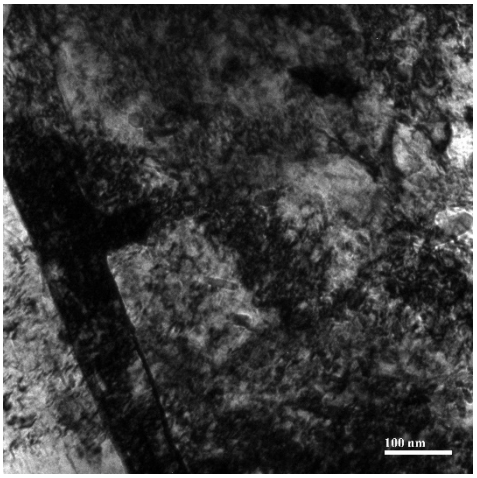

Fig. 4 (a). TEM images of specimens deformed at -195°C and strain rates of 2500 s^{-1}.

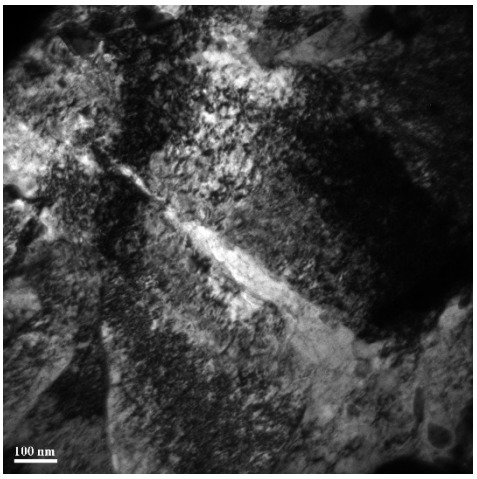

Fig. 4 (b). TEM images of specimens deformed at -195°C and strain rates of 4000 s^{-1}.

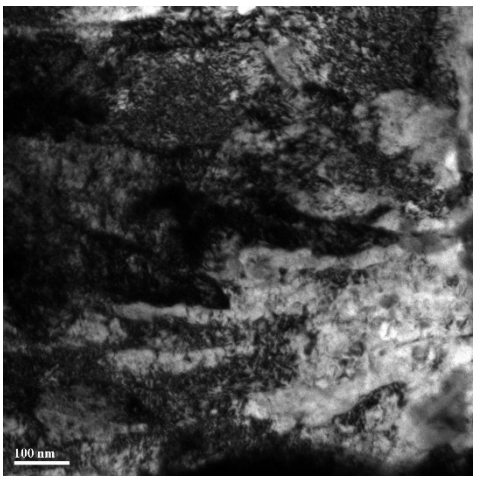

Fig. 4 (c). TEM images of specimens deformed at -195°C and strain rates of 6000 s^{-1}.

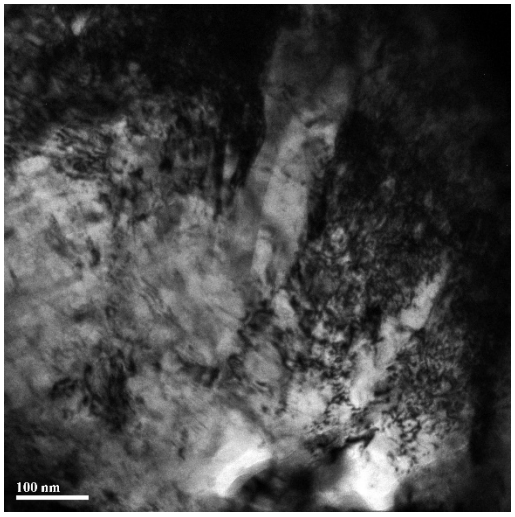

Fig. 5 (a). TEM images of specimens deformed at 25°C and strain rates of 2500 s^{-1}.

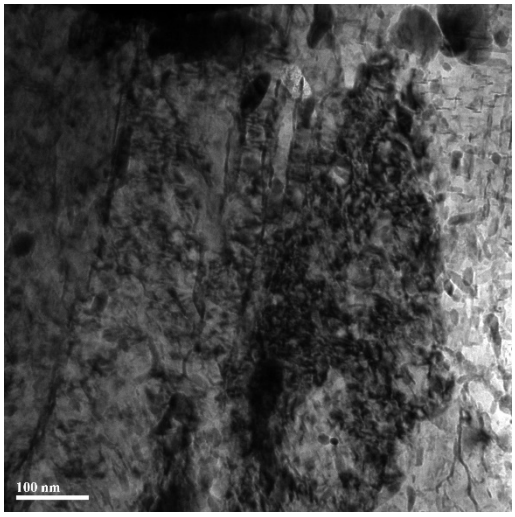

Fig. 6 (b). TEM images of specimens deformed at 400°C and strain rates of 4000 s^{-1}.

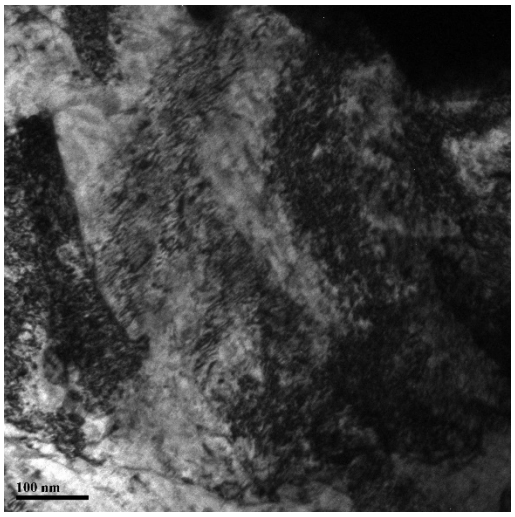

Fig. 5 (b). TEM images of specimens deformed at 25°C and strain rates of 4000 s^{-1}.

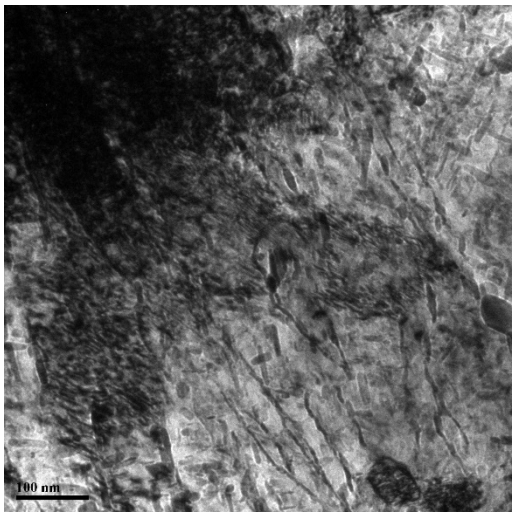

Fig. 7 (a). TEM images of specimens deformed at 800°C and strain rates of 2500 s^{-1}.

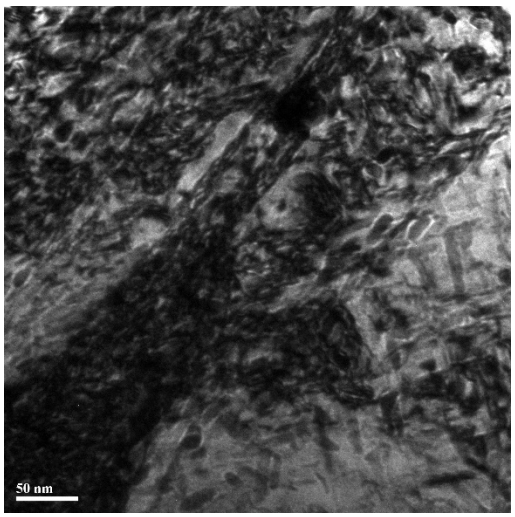

Fig. 6 (a). TEM images of specimens deformed at 400°C and strain rates of 2500 s^{-1}.

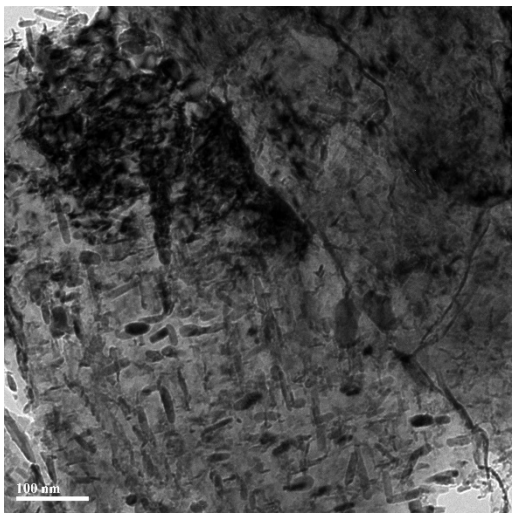

Fig. 7 (b). TEM images of specimens deformed at 800°C and strain rates of 4000 s^{-1}.

Microstructures of ASP 60 Samples Subject to Quasi-Static Deformation

The TEM images in Figures. 8~11 show that the microstructures deformed under quasi-static conditions consist mainly of primary carbide precipitates and fine secondary carbide precipitates. The deformed microstructures are very different from those of the specimens tested under dynamic strain rates, which consist mainly of multiplied dislocation structures (Figs. 4~7). The average size of the precipitates in the quasi-static specimens is also found to be larger than that in the dynamic impact specimens. For example, the carbides in the quasi-static deformation microstructures have diameters of around 50 nm (Figs. 8 and 10), while the secondary carbides in the dynamic deformation microstructures have a fine, rod-like structure (Figs. 5 and 7). Furthermore, the quasi-static microstructure contains both primary carbides and secondary carbides embedded randomly in the matrix with no specific orientations.

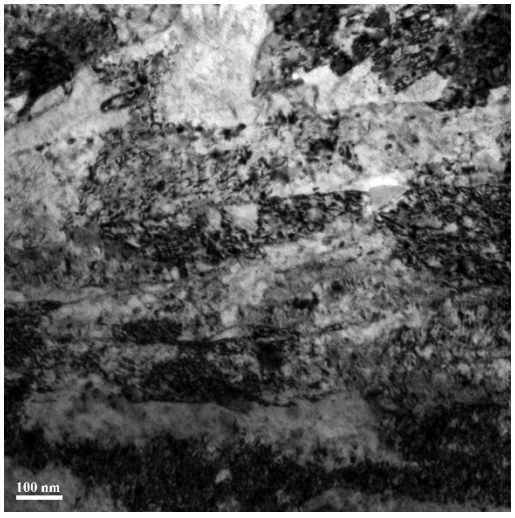

Fig. 8 (a). TEM images of specimens deformed at 25°C and strain rates of 10^{-3} s^{-1}.

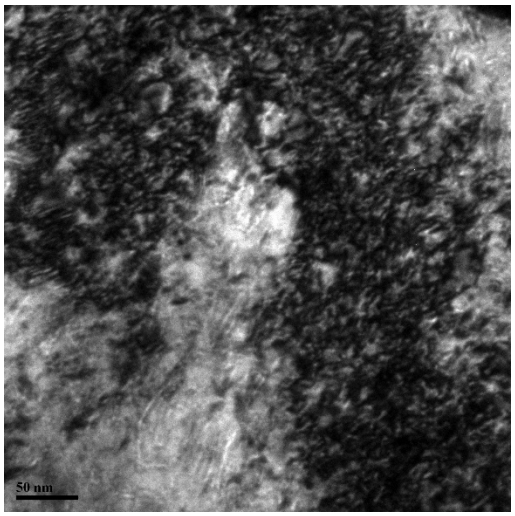

Fig. 8 (b). TEM images of specimens deformed at 25°C and strain rates of 10^{-1} s^{-1}.

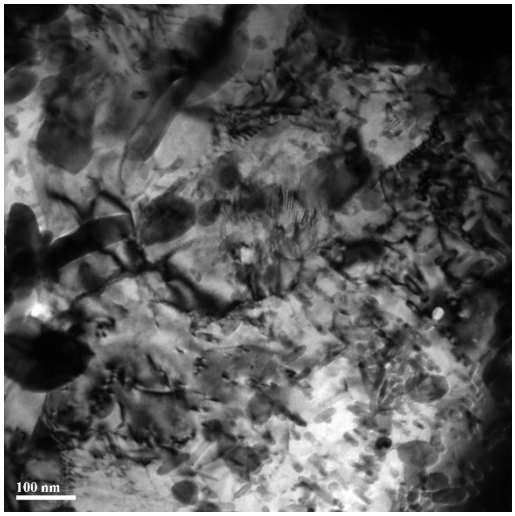

Fig. 9. TEM images of specimens deformed at 700°C and strain rates of 10^{-3} s^{-1}.

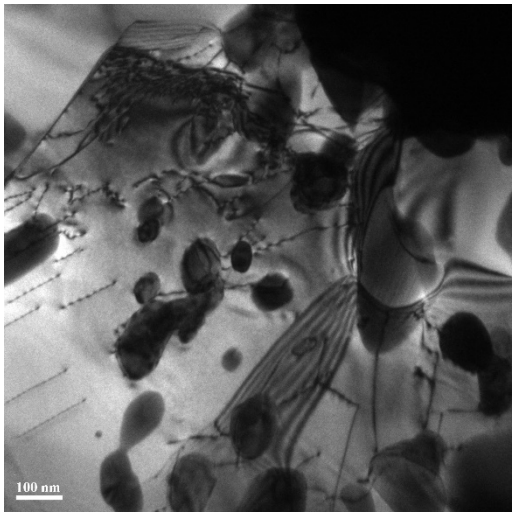

Fig. 10 (a). TEM images of specimens deformed at 800°C and strain rates of 10^{-3} s^{-1}.

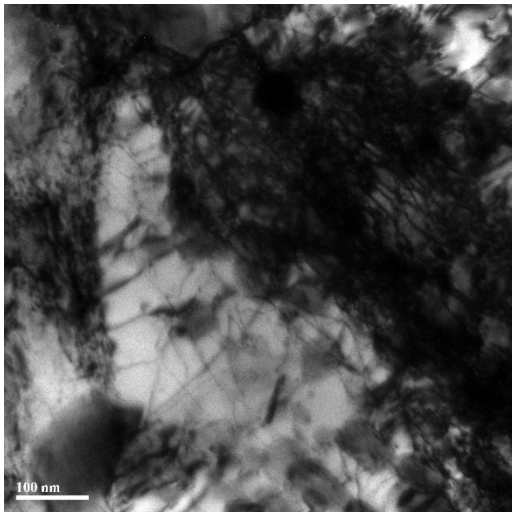

Fig. 10 (b). TEM images of specimens deformed at 800°C and strain rates of 10^{0} s^{-1}.

The deformation temperature has a significant effect on the precipitates and the martensite structures of the specimens deformed under quasi-static loads. At a temperature of 25°C, the microstructure is dominated by fine secondary carbides, which precipitate both at the boundaries of the martensite laths and within the laths themselves (Fig. 8(a)). However, at a higher temperature of 700°C, large primary carbides co-exist with these fine secondary carbides, as shown in Fig. 9. Moreover, at 800°C, the fine secondary carbides diminish in both size and number. Part of the plate martensite matrix transforms into equiaxed grained ferrite structures (Fig. 10(a)). At the highest deformation temperature of 1000°C, even the coarse primary carbides diminish. Heavily twinned martensite and retained austenite are shown at a strain rate of 10^{-3} s^{-1} (Fig. 11(a)). In addition, at the maximum strain rate of 10^{0} s^{-1}, the dislocation clusters and precipitates are no longer finely dispersed, but are strongly concentrated in localized regions, as shown in Fig. 11(b).

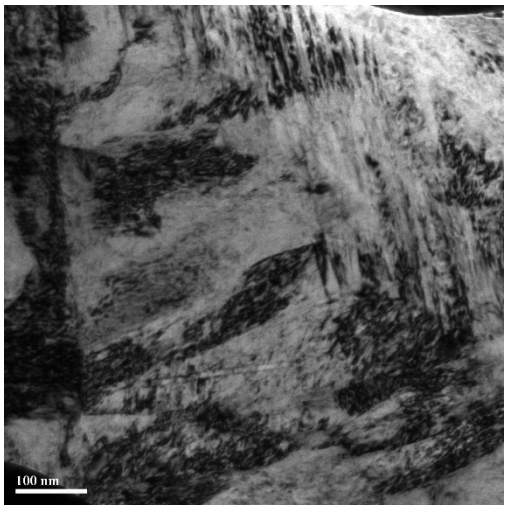

Fig. 11 (a). TEM images of specimens deformed at 1000°C and strain rates of 10^{-3} s^{-1}.

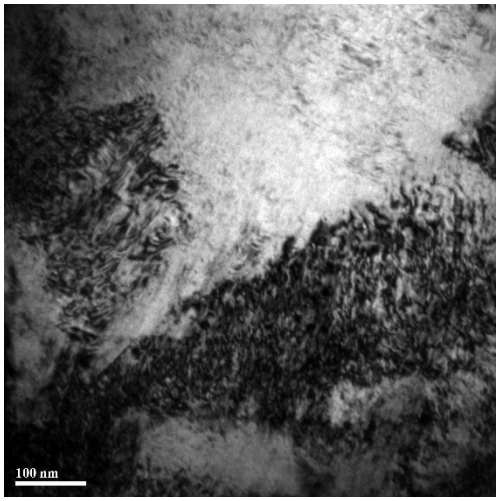

Fig. 11 (b). TEM images of specimens deformed at 1000°C and strain rates of 10^{0} s^{-1}.

Figures 8~11 also show that the clusters of dislocations increase with the strain rate under constant deformation temperatures. For example, as shown in Fig. 8(a), the matrix of the martensite laths in the sample tested at 25°C and a strain rate of 10^{-3} s^{-1} shows less intertwined dislocations. However, under a higher strain rate of 10^{-1} s^{-1}, multiplied dislocations and precipitates are clearly seen. Similarly, for the highest deformation temperature of 800°C, the specimen deformed at a strain rate of 10^{-3} s^{-1} contains only several dislocation lines together with a small number of primary carbide precipitates (Fig. 10(a)), whereas at an increased strain rate of 10^{0} s^{-1}, piles of multiplied dislocations and carbides dominate the microstructure (Figs. 10(b) and 11(b)).

Dislocation Density

The dislocation density in deformed microstructures can be determined from a TEM image marked with five randomly-oriented straight lines as follows (Ham, 1961):

$$\rho = 2n/Lt \quad (7)$$

, where ρ is the dislocation density, L is the total length of the five lines, t is the thickness of the foil, and n is the total number of intersections between the lines and the dislocations. Figure 12 shows the variation of the work hardening stress (σ-σ_y) as a function of the square root of the dislocation density ($\rho^{1/2}$) for the present ASP 60 specimens, where σ is the flow stress and σ_y is the yield stress. For each deformation temperature, the work hardening stress increases linearly with the square root of the dislocation density. In addition, the square root of the dislocation density decreases with increasing temperature. The results are thus consistent with the reduction in flow stress with increasing temperature observed in Fig. 3.

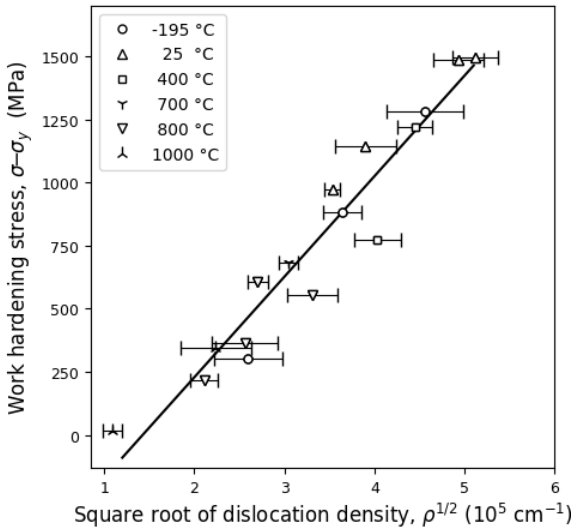

Fig. 12. Variation of work hardening stress with square root of dislocation density at different temperatures.

CONCLUSIONS

Dynamic impact tests and quasi-static deformation tests have been conducted to investigate the effects of the strain rate (1.0×10^{-3} s^{-1} ~ 6.0×10^{3} s^{-1}) and temperature (-195~1000ºC) on the mechanical properties, dislocation microstructures, and precipitation behaviour of high alloyed powder metallurgical high-speed steel ASP 60. The results have shown that the plastic deformation response of the specimens depends strongly on both the strain rate and the temperature. The flow stress decreases with increasing strain rate under sub-zero temperatures (-195ºC) and high temperatures (800ºC) due to the high interfacial area of the powder metallurgic structure. The TEM observations have shown that the dislocation density increases with increasing strain rate but decreases with increasing temperature. The TEM observations have also revealed that the fine precipitates in the ASP microstructure are free from coarsening but are orientated in certain directions under dynamic impacts at a high temperature of 800°C. Finally, the work hardening stress increases linearly with an increasing square root of the dislocation density at each of the considered deformation temperatures.

ACKNOWLEDGEMENTS

The authors gratefully acknowledge the National Science and Technology Council of Taiwan for the financial support provided to this study under Project No. MOST 111-2221-E-239-018.

REFERENCES

ASSAB Group, "ASSAB ASP 60 Datasheet", URL: http://cdna.terasrenki.com/ds/1.3241_1.3292_HS6-7-6-10_SS-2727_Vanadis_60_ASP-60_Datasheet_1.pdf, (accessed 2020-05-25).

D. Hull and D. J. Bacon, Introduction to Dislocations, p. 238, 2011.

H-O. Andrén, "Atom-probe microanalysis of a tempered high-speed steel," Scr. Metall., vol. 15, pp. 749-752, 1981.

J. Härle, P. Lamparter and S. Steeb, "X-ray diffraction study of precipitation in melt-spun high speed steels," J. Phys. IV France., vol. 03, pp. C8-307 - C8-310, 1993.

K. Stiller, L-E. Svensson, P. R. Howell, W. Rong, H-O. Andrén and G. L. Dunlop, "High resolution microanalytical study of precipitation in a powder metallurgical high speed steel," Acta. Metall., vol. 32, pp. 1457-1467, 1984.

M. A. Gomes, A. S. Wronski and C. S. Wright, "Fractue behaviour of a highly alloy high speed steel," Fatigue Fract. Engng. Mater. Struct. vol. 18 pp. 1-18, 1995.

P. L. Tso and C. C. Lu, "Study on the grinding of P/M high speed steel ASP 60," Int. J. Mach. Tools Manuf. vol. 39, pp. 627–638, 1999.

P. S. Follansbee and U. F. Kocks, "A constitutive description of the deformation of copper based on the use of the mechanical threshold stress as an internal state variable," Acta. Metall., vol. 36, pp. 81-93, 1988.

R. K. Ham, "The determination of dislocation densities in thin films," Philos. Mag. A., vol. 6, pp. 1183-1184, 1961.

R. M. German, Powder Metallurgy Science, pp. 150-151, 1994.

S. H. Chang, C. L. Huang, K. T. Huang and C. M. Liu, " Improvement of the wear and corrosion behaviors of DLC oxynitriding duplex-treated PM60 High-speed steel via various power densities of DC-pulsed plasma enhanced CVD," ISIJ Int., vol. 56, pp. 2276-2283, 2016.

W. Rong, H. O. Andren, H. Wisell and G. L. Donlup, " The role of alloy composition in the precipitation behaviour of high speed steel," Acta Metall. Mater., vol. 40, pp. 1727-1738, 1992.

W. S. Lee and C. Y. Liu, "The effects of temperature and strain rate on the dynamic flow behaviour of different steels," Mater. Sci. Eng. A., vol. 426, pp. 101–113, 2006.

W. S. Lee, T. H. Chen and H. H. Hwang, "Impact response and microstructural evolution of biomedical titanium alloy under various temperatures," Metall. Mater. Trans. A. Phys. Metall. Mater. Sci., vol. 39, pp. 1435-1448, 2008.

W. S. Lee and Z. C. Tang, "Relationship between mechanical properties and microstructural response of 6061-T6 aluminum alloy impacted at elevated temperatures," Mater. Des., vol. 58, pp. 116-124, 2014.

應變速率及溫度在粉末冶金高速鋼(ASP 60)變形行為與微觀結構上的效應分析 Part 2—微觀結構

李偉賢
國立聯合大學機械工程學系

陳亭儒
國立成功大學機械工程學系

摘要

本文旨在研究粉末冶金高速鋼 ASP 60 之動態衝擊

與準靜態的變形行為。透過萬能材料試驗機和霍普金森衝擊試驗機，我們在溫度範圍為-195˚C至1000˚C，應變速率為10^{-3}至10^{0} s^{-1}，以及2.5×10^{3}至6.0×10^{3} s^{-1}的條件下進行變形實驗。研究結果顯示，粉末冶金高速鋼 ASP 60在動態衝擊下，其流變應力隨著溫度下降和應變速率增加而呈現上升的趨勢。同時，由於材料內部的粉末燒結特性，粉末冶金高速鋼 ASP 60在特定應變速率與溫度展現負的應變率敏感性係數值。觀察變形之材料顯微組織，發現粉末冶金高速鋼 ASP 60在-195˚C至25˚C和2.5×10^{3}至6.0×10^{3} s^{-1}的條件下，材料內部差排組織嚴重糾結叢集，而此現象亦促使粉末冶金高速鋼 ASP 60於變形過程中呈現高塑流阻抗。而無論處於動態衝擊或準靜態變形，粉末冶金高速鋼 ASP 60的差排糾結密度對溫度和應變速率均呈現極高的敏感性。分析動態衝擊試件之微觀影像，發現其晶粒析出物尺寸比準靜態試件中的析出物更加微細。最後結合微觀及巨觀性質，可以得到塑流應力值與差排密度平方根呈線性關係。